IEEE Journal of Microwaves

MTT-S
MHz to THz Community

Received 3 December 2020; revised 2 February 2021, 24 February 2021, and 27 February 2021; accepted 28 February 2021. Date of publication 29 March 2021; date of current version 7 April 2021.

Digital Object Identifier 10.1109/JMW.2021.3063510

Circuit-on-Display: A Flexible, Invisible Hybrid Electromagnetic Sensor Concept

JUNHO PARK [1], **DONGPIL PARK** [2], **MYUNSOO KIM** [2], **DOOCHAN JUNG** [3], **CHISANG YOU** [3], **DOOSEOK CHOI** [4], **JONGWOO LEE** [4], **AND WONBIN HONG** [1]

(Regular Paper)

[1]Department of Electrical Engineering, Pohang University of Science and Technology, Pohang 37673, Republic of Korea
[2]Sensor Research and Development Center, Dongwoo Fine-Chem, Pyeongtaek 17956, Republic of Korea
[3]Mobile Communication Division, LG Electronics, Seoul 07796, Republic of Korea
[4]S.LSI Division, Samsung Electronics, Hwasung 18448, Republic of Korea

CORRESPONDING AUTHOR: Wonbin Hong (e-mail: whong@postech.ac.kr).

This work was supported in part by the Basic Science Research Program through the National Research Foundation of Korea (NRF) funded by the Ministry of Education under Grant 2019R1A6A3A13096306; in part by the Institute of Information and Communications Technology Promotion (IITP) funded by the Korean Government (MIST) under Grants 2018-0-00733 and 2020-0-00858; and in part by Dongwoo Fine-Chem, LG Electronics, and Samsung Electronics S.LSI Division via the SPRC program.

ABSTRACT There have been scarce interactions between microwave circuits and display technologies over the past few decades. However, the two share many similarities leaving room for integration and co-development. Hence, we present a Circuit-on-Display (CoD) concept that dually functions as a radio-frequency transceiver and a high-resolution touch screen display. The approach is realized through a flexible, invisible hybrid electromagnetic sensor (HEMS) which is situated inside a high-resolution display panel. The CoD is integrated within a real-life millimeter-wave 5G NR Android-based cellular handset prototype to demonstrate a foreside beamforming coverage and a touch operation with high-resolution and optimal image quality. The devised HEMS prototype independently features flexibility, optically invisibility (transmittance $>88\%$), and multi-functionality (system gain of 20.72 dB, beam scanning range of $\pm 40^\circ$, and mutual capacitance change ratio $>4.42\%$). The devised approach provides a new class of approach to enable microwave integrated circuits for new generation wireless electronics.

INDEX TERMS Beamforming, capacitive sensors, fifth-generation (5G) communication, massive multiple-input multi-output (MIMO), millimeter-wave, phased-array, sixth-generation (6G), transceiver .

I. INTRODUCTION

The advent of displays featuring surface-integrated touch sensors revolutionized the electronics industry over the past two decades [1]. Displays with touch input capabilities not only provide information in visual form but also enable users to directly interact with devices. Moreover, this information from users and devices can be shared via wireless communication protocols such as Bluetooth, Wi-Fi, 3G, 4G, and 5G standards [2]–[6]. Naturally, every device should be equipped with radio frequency (RF) transceiver modules which include monolithic microwave integrated circuits (MMIC) and antennas. In addition, it is expected that a plural number of antennas and MMICs will be required for upcoming massive multi-input multi-output (MIMO) antenna technologies to further enhance channel capacities of future wireless links [7]–[10].

Electromagnetic waves cannot propagate through metallic boundaries. Naturally, antennas and MMICs have been placed in the areas outside the display components containing metallic parts for all wireless devices such as laptop, TV, portable devices [11]–[16]. For instance, for long-term evolution (LTE) RF front-end modules, the metallic rim is utilized as the antenna to minimize the required real-estate [11]–[13]. In the case of millimeter-wave 5G cellular devices, multiple antenna-in-package (AiP) modules are placed within the bezel area [14] and the back cover [15]–[16] region of cellular handsets. In addition, the recent proliferation of cloud computing and ultrafast wireless communication has introduced new display-driven designs featuring full-screen, higher resolution, and new form factors such as wearable, curved, rollable, and foldable displays [17]–[20]. Collectively it is clear that there will be less space available for wireless circuits while the wireless technological requirements become increasingly stringent. This introduces an unprecedented, critical tradeoff between the design and wireless capability of upcoming wireless devices.

Recently, alternative approaches for embedding the optically transparent antenna on display (AoD) components have been proposed [21]–[24]. In these approaches, a conductive antenna layer is integrated between the front glass and the light-emitting device of display components. However, these AoD configurations have omitted the presence of the touch sensor layer due to the inherent challenges related to the coexistence of two conductive touch-sensor and antenna layers. 1) From the antenna perspective, other metallic objects (e.g., a touch sensor layer) located in close proximity of the antenna increase the capacitively stored energy of the radiation reactance, which results in reduction of the antenna radiation efficiency. Moreover, if the touch sensor layer is positioned above the radiation direction of the antenna, the radiated energy from the antenna layer is significantly blocked by the touch electrode layer. 2) From the touch sensor perspective, a separate metallic layer (antenna layers) located near the touch sensors dramatically reduces the mutual capacitance change ratio [25], which is highly correlated to touch sensitivity, according to the presence or absence of fingers. In addition, the presence of two separate electrode layers not only reduces the entire optical transparency of display components but also causes visual quality issues such as Moiré and haze [26] due to the spatial frequency difference between two different periodic-patterned layers. Considering the fact that present-day cellular devices have to be equipped with display-integrated touch sensors, this configuration limits the potential level of integration and functional expansion. In [27], [28], several traditional touch-sensor panel (TSP) geometries are engineered as frequency selective surfaces (FSSs) at microwave frequencies to enable the transmission of electromagnetic waves from and towards the antennas situated on a separate layer. Although simulated results demonstrate the feasibility of the coexistence of the touch sensor and antenna layers, the aforementioned challenges still remain due to the use of two separate conductive layers. In addition, the operating frequency of the FSS structure is inherently narrow, which is problematic for wideband millimeter-wave and terahertz wireless applications.

In this article, we propose a new concept denoted as Circuit-on-Display (CoD) which attempts to integrate wireless circuits on the same layer of the touch screen sensors of display panels for the first time. We exemplify this concept using a flexible, invisible hybrid electromagnetic sensors (HEMS) architecture incorporating optically invisible antennas and touch sensors as presented in Fig. 1(a). The unique HEMS patterns consisting of mesh-shaped unit cells are devised on cyclo olefin polymer (COP) film using conductive metallic alloys. The CoD prototype with the HEMS is fabricated using photolithography and fully integrated within an organic light–emitting diode (OLED) display panel. We further construct a real-life cellular handset prototype with the fully integrated CoD prototype which functions as millimeter-wave (mmWave) 5G new radio (NR) beamsteering RF transceivers as well as high-resolution (WQHD+) touch screen display.

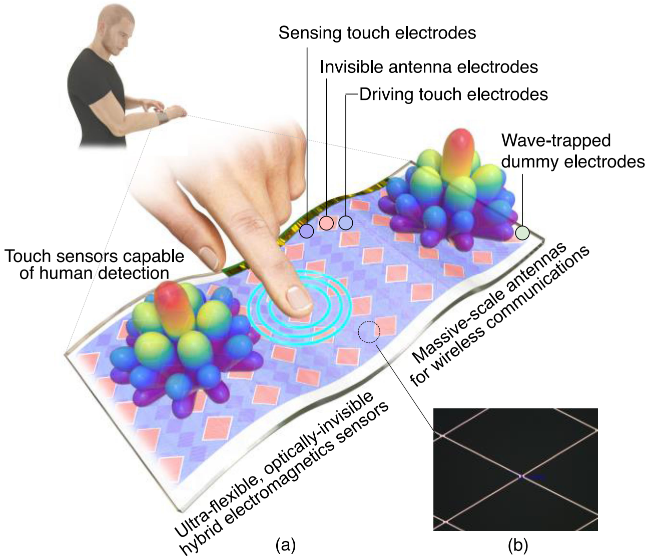

FIGURE 1. **(a) Illustration of the CoD concept for future wearable devices. (b) Microscopic photograph of the CoD POC containing diamond-grid patterned electrodes.**

This article is organized as follows. Section II introduces the operating mechanism of the proposed CoD concept and the implementation method considering packaging, integration, and material aspects. The detailed design process of each functional block is described in Section III. The CoD proof-of-concept (POC) is designed to prove the feasibility of the proposed concept in Section IV. The measured and simulated results of the prototype are discussed in Section V. The concluding remark is provided in Section VI.

II. PRINCIPLE AND IMPLEMENTATION

The exemplified design of the CoD system using the flexible, invisible HEMS architecture is shown in Fig. 1(a). The HEMS architecture contains three functional blocks comprising of antenna electrodes, driving/sensing touch sensor electrodes, and wave-trapped dummy electrodes, all of which are coherently arranged on a single layer.

A. HEMS ARCHITECTURE

The systematic HEMS architecture is illustrated in Fig. 2. The invisible touch sensor/antenna patterns are intertwined in a lattice form and placed on the identical layer. Independent signal paths for each circuit enable simultaneous and respective transmission of RF and touch signals. Independently adjusted gain and phase of the RF signals from the MMICs allow the adaptive beamforming operation of the active phased array antennas. We adopt an orthogonal cross-shaped touch electrode as the basic structure to reduce the design parameters and enable a robust arrangement with the

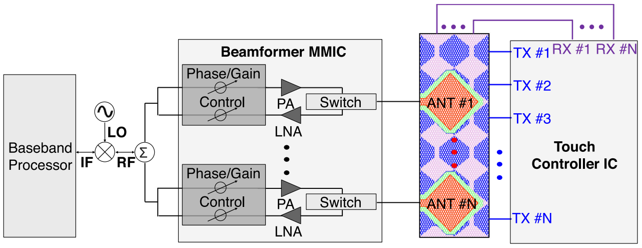

FIGURE 2. **Schematics of the HEMS architecture including the touch controller IC and the beamformer MMIC.**

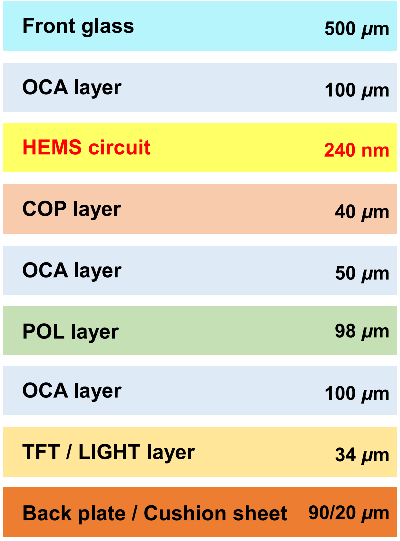

Layer	Thickness
Front glass	500 μm
OCA layer	100 μm
HEMS circuit	240 nm
COP layer	40 μm
OCA layer	50 μm
POL layer	98 μm
OCA layer	100 μm
TFT / LIGHT layer	34 μm
Back plate / Cushion sheet	90/20 μm

FIGURE 3. **Stack-up of the display-integrated HEMS (OCA = optically clear adhesives, HEMS = hybrid electromagnetic sensor, COP = cyclo olefin polymer, POL = polarizer, and TFT = thin-film transistor).**

integrated invisible antenna. In this HEMS design, multiple invisible antenna elements can be formed without overlapping with driving/sensing traces in the vertical and horizontal axes of the invisible touch sensors. The entire HEMS circuit is implemented using conductive mesh alloy unit cells featuring a line width of 2.5 μm and a thickness of 2400 Å for maximal optical transparency, as illustrated in Fig. 1(b).

B. MATERIALS AND PROCESS

A photolithography process is used to implement the HEMS circuit consisting of diamond-grid shaped unit cells. A conductive mesh Cu-alloy featuring a thickness of 2400 Å, a width of 2.5 μm, and a surface resistivity of 5 Ω/sq is used to construct diamond-grid shaped unit cells. The conductive Cu-alloy is first deposited on the temporary substrate using DC sputtering process. Afterward, a photoresist layer is deposited on the conductive Cu-alloy layer. UV light is applied to the patterned mask featuring the diamond-grid shaped pattern on the PR layer. A portion of the conductive mesh Cu-alloy region is chemically etched according to the patterned mask. After the remaining PR is removed using a strip process, the diamond-grid patterned conductive mesh Cu-alloy layer is formed on the temporary substrate. This temporary substrate is removed using a transfer process and replaced with a 40 μm-thick COP film. Finally, the COP layer and other required layers (e.g., front glass, polarizer, etc.) are laminated together using three optically clear adhesive (OCA) films, as illustrated in Fig. 3. A front glass substrate featuring a relative dielectric constant of 6.8 and a thickness of 500 μm is used to protect the conductive mesh Cu-alloy from mechanical damages and oxidization. The thin-film transistor (TFT) and emitting layers of the OLED display panel function as an electrical ground for antennas of the HEMS circuit.

III. HEMS CIRCUIT DESIGN AND BUILDING BLOCK MEASUREMENTS

When devising the HEMS circuit, it becomes imperative for antenna electrodes and touch sensor electrodes to function independently amid extremely close proximity on a single layer. It is worth noting that in the case of conventional touch sensor electrodes cross talk and signal interference become inevitable due to the inherent topology. Conventional touch sensors [25] consist of driving/sensing electrodes and ITO bridges which are used to connect the sensing electrodes at the overlapping regions between the driving and sensing electrodes. When a touch contact is detected on the TSP, the electric field distribution between the driving and sensing electrodes is altered by the introduction of a new current path originating from the touch objects. This deviation in the electric field distribution changes the mutual capacitance between the driving and sensing electrodes, which validates the touch action. The mutual capacitance change ratio is defined as

$$\frac{\Delta C_M}{C_M} = \frac{C'_M - C_M}{C_M} \tag{1}$$

Where C_M denotes the equivalent mutual capacitance between the driving and sensing electrodes under consideration and C'_M is the corresponding mutual capacitance with the presence of the touch object. However, in the case of conventional TSPs, the addition of the antenna trace will overlap with the ITO bridges at the junctions, ultimately disabling the driving/sensing touch traces. In addition, the mutual capacitance change ratio is significantly affected by the reduced effective area of the touch sensor when the antenna is inserted into the surface of the unit cell of the touch sensor. A quad-patterned touch sensor topology (see Fig. 4) is devised to enable the interconnection of each driving/sensing traces with the coexistence of the antenna electrodes while mitigating reduction of the mutual capacitance change ratio between the driving/sensing traces.

The entire HEMS circuit (see Fig. 5(a), 5(b), and 5(c)) is composed of unit cells featuring a width (W_{unit}) of 4.35 mm and a length (L_{unit}) of 4.15 mm in consideration of scan time [29] required for touch sensor panels. It is noted that the antenna and dummy electrodes can either be completely integrated within a single unit cell or be divided and placed across

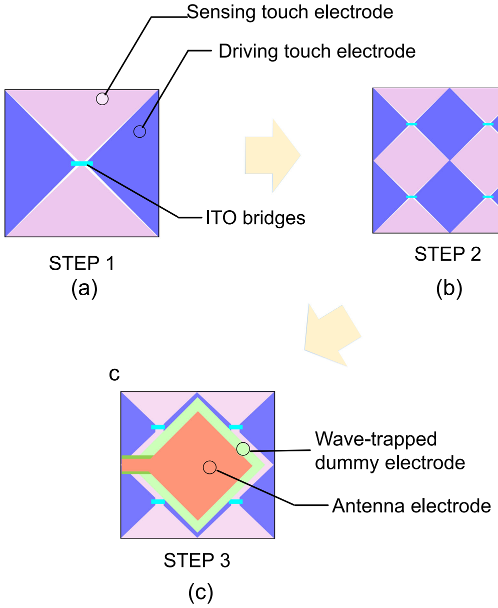

FIGURE 4. **Conceptual illustration of devising a HEMS topology. (a) The unit cell of the conventional touch sensors. (b) The unit cell of the proposed quad-patterned touch sensors. (c) The unit cell of the proposed HEMS incorporating sensing/driving touch electrodes, wave-trapped dummy electrodes, and antenna electrodes.**

multiple cells. Hence, the HEMS architecture is compatible with any antenna topologies and antenna array configurations due to its modular nature. The unit cells of the HEMS circuit constitute identical and periodic diamond-grid mesh structures featuring a line width (W_{cell}) of 2.5 μm, a mesh width (H_{cell}) of 131 μm, and a mesh height (V_{cell}) of 248 μm, as illustrated in Fig. 5(d). The dimension of this diamond-grid mesh structure can be further modified in accordance to the characteristics of emitting layers within display panels. Therefore, each functional block exhibits an identical spatial frequency through the aforementioned arrangement of the mesh patterns. Consequently, the presence of the HEMS circuit does not cause any visual quality degradation such as Moiré and haze [26] when placed above OLED displays or liquid crystal displays (LCDs). The final dimensions of the diamond-grid mesh structure are determined based on numerical analysis to optimize the trade-off between the optical transparency and RF sheet resistance. The measured optical transparency (Fig. 6) in the area containing the HEMS circuit features more than 88% which is acceptable for modern commercial applications. The optical transparency of the CoD POC is measured using a Konica Minolta CM-3700A spectrophotometer.

A. ANTENNA ELECTRODES

A diamond-shaped patch radiator is selected for an antenna topology to be physically compatible with the quad-patterned touch sensor topology. The operating principle of the diamond-shaped patch radiator is identical to that of conventional patch antennas which contain two radiating magnetic currents (J_{M1} and J_{M2}) at the edges along the x-axis, as illustrated in Fig. 7. The diamond-shaped patch radiator of the HEMS circuit is designed to operate at a center frequency of 28 GHz while exhibiting a vertically polarized broadside radiation pattern. The operating frequency of diamond-shaped patch radiator is optimized by physically adjusting the length of the radiator ($L_{HS} = 3.5$ mm), and the impedance matching is performed by controlling the width of the radiator ($W_{HS} = 3.47$ mm). In the CoD POC, each radiator is uniformly spaced with an increment of 6.23 mm, taking into account the isolation between the elements and the beam scanning range. The stacked dielectric layer (see Fig. 3) between the radiator (HEMS layer) and the ground plane (TFT layer) can be equivalently modeled as a single dielectric layer with a thickness of 288 μm, a relative permittivity of $\varepsilon_r = 2.8$, and a loss tangent of $tan\delta = 0.01$. The feedline of the diamond-shaped patch radiator is routed and connected with the transmission lines on the FPCB consisting of a single LCP substrate layer featuring a thickness of 50 μm, a relative permittivity of $\varepsilon_r = 3$, and a loss tangent of $tan\delta = 0.0008$. The anisotropic conductive film (ACF) bonding process is used to create electrical interconnection between the HEMS circuit and the RF/touch sensor packages.

To accurately characterize the antenna of the HEMS circuit, the feedline of the two antenna elements is routed to the T-junction power divider on the FPCB. RF signal feeding is established at the end of the FPCB to confirm the input impedance of the antenna. The electromagnetic simulator, Ansys HFSS, is used to extract the input impedance and the far-field properties of the antenna of the HEMS circuit. The measured input impedance bandwidth (reflection coefficient <-10 dB) of the antenna of the HEMS circuit features 1.53 GHz with a center frequency of 27.93 GHz, as illustrated in Fig. 8(b). To evaluate the radiation properties of the antenna of the HEMS circuit, the CoD POC is positioned above the jig which is placed within the mmWave far-field anechoic chamber as illustrated in Fig. 8(a). It is confirmed from Fig. 8(c) that high correlation is achieved between the simulated and measured radiation patterns in the yz-plane. The measured and simulated peak realized gain (Fig. 8(d)) is 2.48 dBi and 2.31 dBi at 27.5 GHz, respectively. The calculated measured efficiency (Fig. 8(e)) of the antenna of the HEMS circuit features approximate 40% at 28.5 GHz despite the inclusion of lossy dielectric materials and insertion losses of transmission lines on the FPCB. The discrepancy between simulated and measured results is mainly attributed to the manufacturing tolerances, the deviation of the substrate electrical characteristics, and the lack of detailed modeling of the actual device. In addition, it is worth noting that the radiation properties of antennas may deviate if the ground area is wider than the size of that of the designed antenna or if metallic components that have not been considered exist adjacent to the antennas.

B. TOUCH SENSOR ELECTRODES

Considering the fact that all relevant capacitances of the touch sensor panel can be captured by electroquasistatic simulation of a small panel section due to its periodicity [30], the 5 × 5

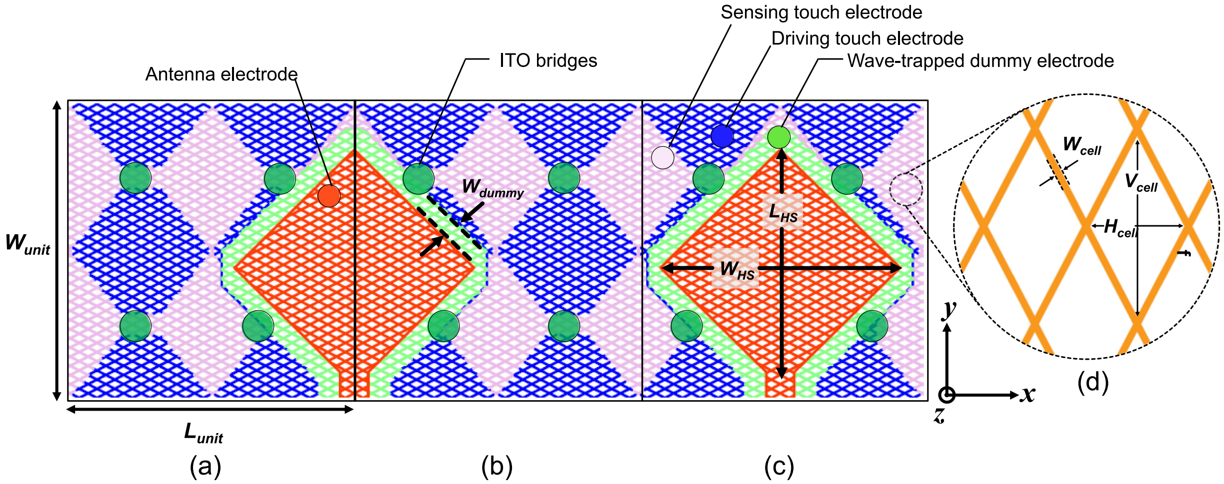

FIGURE 5. **(a) The HEMS unit cell containing the left half of the antenna and dummy electrodes. (b) The HEMS unit cell containing the right half of the antenna and dummy electrodes. (c) The HEMS unit cell containing the entire antenna and dummy electrodes. (d) Magnified image of the HEMS unit cell containing diamond-grid patterned electrodes. Note that all electrodes are placed on a single layer.**

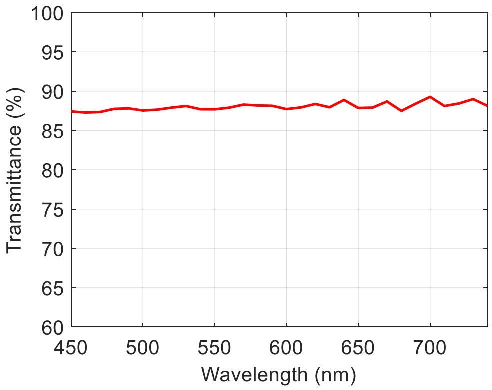

FIGURE 6. **Measured optical transparency in the area containing the HEMS circuit.**

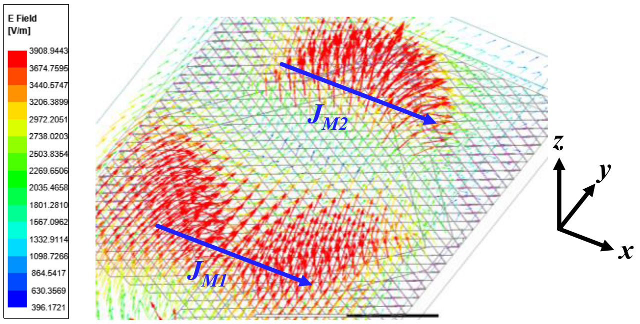

FIGURE 7. **E-field distribution of the HEMS circuit when the feedline of the antenna element is fed at 28 GHz.**

HEMS unit cells are verified with consideration of the entire display material composite and stack-up. The touch sensor of the HEMS circuit is characterized using the electroquasistatic simulator, Ansys Q3D. The simulation model with the defined *x*-*y* coordinate is illustrated in Fig. 9. Fig. 10 shows the heat map of the mutual capacitance change ratio of the 5 × 5 HEMS unit cells when the touch object is positioned at (21) in the defined coordinate system. The mutual capacitance change ratio of the HEMS circuit at the position of the touch object features −4.43%. This value is clearly higher than a mean value of −0.25% for the remaining cells. It is noted that the absolute value of the mutual capacitance change ratio is slightly reduced in the area where the antenna and dummy electrodes coexist. However, this value can be calibrated through minor adjustments in the algorithm [31] of the touch controller IC. Nevertheless, it is clearly confirmed that touch impact is detectable for any touch positions regardless of the coexistence of the antenna and dummy-grid electrodes.

C. WAVE-TRAPPED DUMMY ELECTRODES

The conductivity of the display-integrated HEMS electrodes is sufficient to guide unwanted electromagnetic interference (EMI) from external noise sources. In particular, it is well known that the EMI from the display components significantly deteriorates the sensitivity of RF systems [32]–[34]. Therefore, the wave-trapped dummy electrodes featuring a width (W_{dummy}) of 0.31 mm are devised to achieve high noise immunity against external EMI noises. The wave-trapped dummy electrodes are equivalent to the open-circuit boundary, which effectively suppress the near-field coupling [35]. While driven currents can exist on each of the antenna and touch sensor electrodes, the electrodes yield a filtering response and suppress mutual coupling. Fig. 11 illustrates the E-field distribution of the HEMS circuit while the touch signal is excited to the driving electrodes. E-field distributions of the HEMS circuit are calculated using the finite element method based Ansys HFSS. It is clearly confirmed from Fig. 11 that the lower E-field intensity is induced at the antenna electrodes of the HEMS circuit with the wave-trapped dummy electrodes compared to that of the HEMS circuit without the

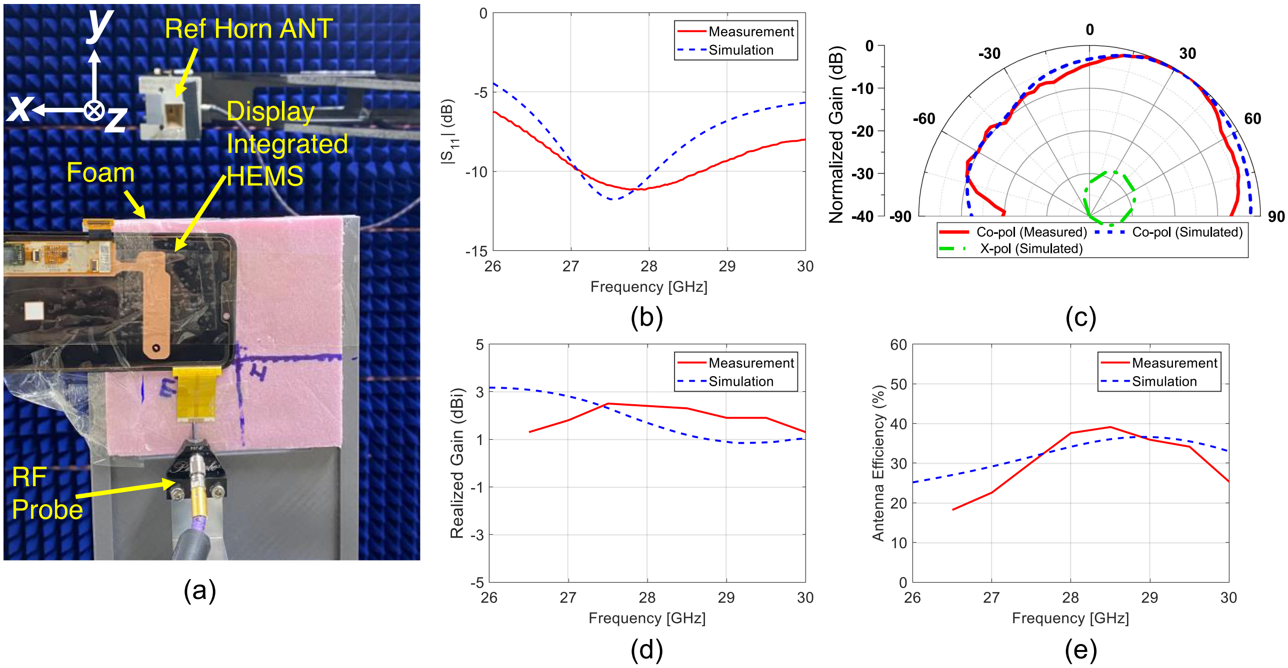

FIGURE 8. Characterization of the antenna electrodes of the display integrated-HEMS circuit. (a) mmWave far-field antenna chamber setup. (b) Measured (red curve) and simulated (blue curve) reflection coefficients of the antenna of HEMS circuit. (c) Measured co-polarized (red curve), simulated co-polarized (blue curve), and simulated x-polarized (green curve) radiation patterns in yz-plane. (d) Comparison of measured and simulated peak realized gain as a function of frequencies. (e) Comparison of measured and simulated total antenna efficiency as a function of frequencies.

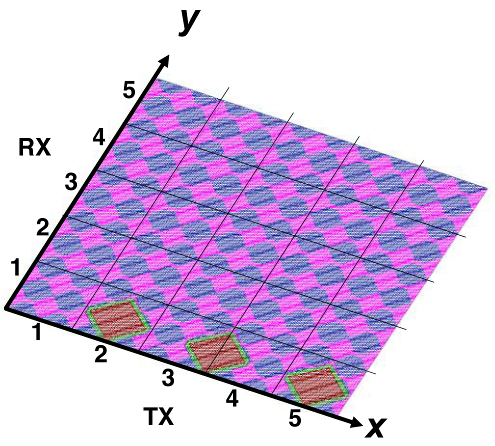

FIGURE 9. Simulation model for the 5 × 5 HEMS unit cells.

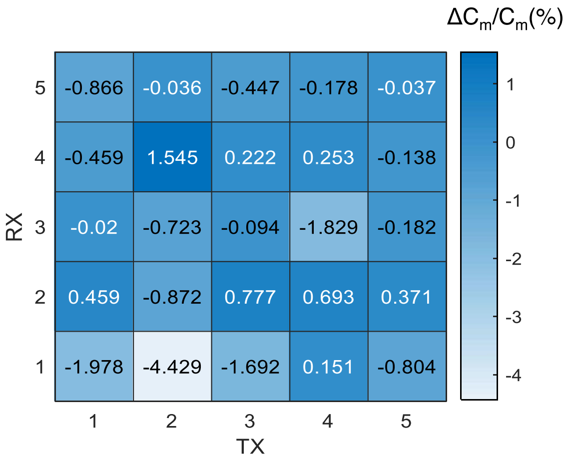

RX \ TX	1	2	3	4	5
5	-0.866	-0.036	-0.447	-0.178	-0.037
4	-0.459	1.545	0.222	0.253	-0.138
3	-0.02	-0.723	-0.094	-1.829	-0.182
2	0.459	-0.872	0.777	0.693	0.371
1	-1.978	-4.429	-1.692	0.151	-0.804

FIGURE 10. Simulated Tx-Rx mutual capacitance change ratio when the touch object is positioned at (2, 1).

wave-trapped dummy electrodes. Therefore, the electromagnetic fields are considerably shielded when the wave-trapped dummy electrodes surround the antenna electrodes, resulting in formation of distinct electrical boundaries.

IV. DEMONSTRATION OF DISPLAY-INTEGRATED HEMS WITHIN A CELLULAR HANDSET PROTOTYPE

The CoD system is demonstrated in a device testbed with an RF package and a touch sensor package. Fig. 12 depicts the fabricated flexible, rollable, and invisible HEMS composite. The OLED display including the HEMS composite is built layer by layer. Fig. 13 illustrates the exploded view of the CoD POC consisting of the RF package, the touch sensor package, and the display-integrated HEMS circuit. To connect with RF input/output (I/O) ports on the external rigid or flexible printed circuit board (FPCB) package, the antenna feeding section of the HEMS circuit is electrically connected with the transmission line on the FPCB. This FPCB supports direct connection with the MMIC and can be integrated with relative ease within devices featuring stringent form factors. The touch feeding section of the HEMS circuit is also routed to the bottom edge side and connected with the semi-rigid printed circuit board (PCB) package including the touch controller IC. The RF package includes the beamformer MMIC, power

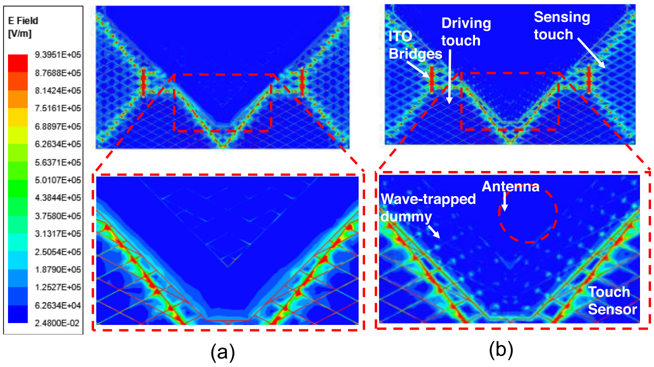

FIGURE 11. **Comparison of E-field distribution of the HEMS circuit. (a) Without the wave-trapped dummy electrodes. (b) With the wave-trapped dummy electrodes.**

FIGURE 12. **Optical photographs of the fabricated HEMS composite for freestanding (top-left), flexed curved (top-right), and rolled (bot-middle) orientations.**

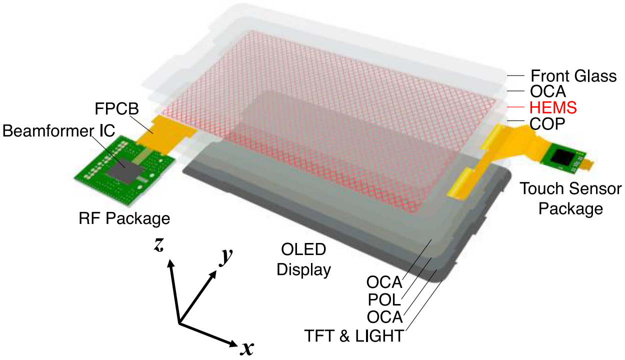

FIGURE 13. **Exploded view of the CoD POC.**

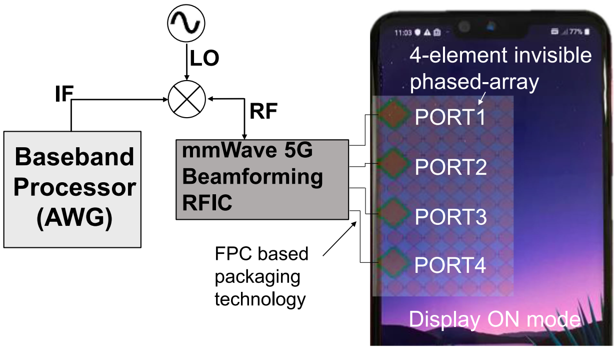

FIGURE 14. **Illustration of the RF measurement setup for the CoD POC integrated within a real-life mmWave 5G NR Android-based cellular handset prototype. Note that the frequency of the LO signals are swept from 26.5 GHz to 29.5 GHz.**

TABLE 1. **Phase Distribution of the RF Port Excitation to Demonstrate Beamforming Capability**

	PORT1	PORT2	PORT3	PORT4	Scanning Angle
BEAM1	0	0	0	0	0°
BEAM2	0	±45°	±90°	±135°	±12°
BEAM3	0	±90°	±180°	±270°	±25°
BEAM4	0	±135°	±270°	±45°	±40°

*All values in degrees

**The power supplied to each port is set to the maximum value.

distribution networks (PDNs), and low/high-speed traces. The beamformer MMIC is mounted on the top side of the RF package. The MMIC is fabricated using 28-nm bulk CMOS technology and designed for 28 GHz 5G new radio (NR) phased-array applications. The beamformer chip directly divides/combines the RF power in RF transmitting (TX)/Receiving (RX) channels using an on-chip Wilkinson divider network. In addition, 3-bit phase shifters and variable gain amplifiers are integrated together within each TRx channel for electronically-controlled beamsteering using high-speed serial interface. The RF power is fed by the external mixer and baseband processor.

The beamformer MMIC featuring a size of 5.47 mm × 3.75 mm is mounted on a PCB using flip-chip ball grid array technology. The RF I/O pads are routed to the edge of the PCB to connect with the radiator's feedline in the HEMS circuit, while the electrical phase of each routing transmission line is thoroughly matched to avoid any requirement (e.g., array calibration) for beamforming operations. A low-frequency 52 MHz clock signal is distributed across the beamformer chip to synchronize each part of the entire MMIC architecture. The on-PCB decoupling capacitors are utilized to satisfy the maximum dynamic current requirements by reducing the impedance of the power distribution network (PDN) of the RF package.

V. TRX PHASED-ARRAY MEASUREMENT

System-level measurements over the air are conducted to assess the beamforming capabilities of the fabricated CoD POC within a real-life mmWave 5G NR Android-based cellular handset prototype (Fig. 14). The calculated input weighting

RF Package (TX mode/4 RF Channels)			FPCB		Estimated RF Package Gain
RF COM line loss*	PA Gain**	Channel line loss	Bond & Mismatch loss	Line loss	
-1.45 dB	+24.9 dB	-1.97 dB	-1.5 dB	-3.30 dB	16.68 dB

NOTE: All value of each component are extracted from the measured results.
* Including 2.92 mm RF connector
** Including power-combing loss in four RF channels

(a)

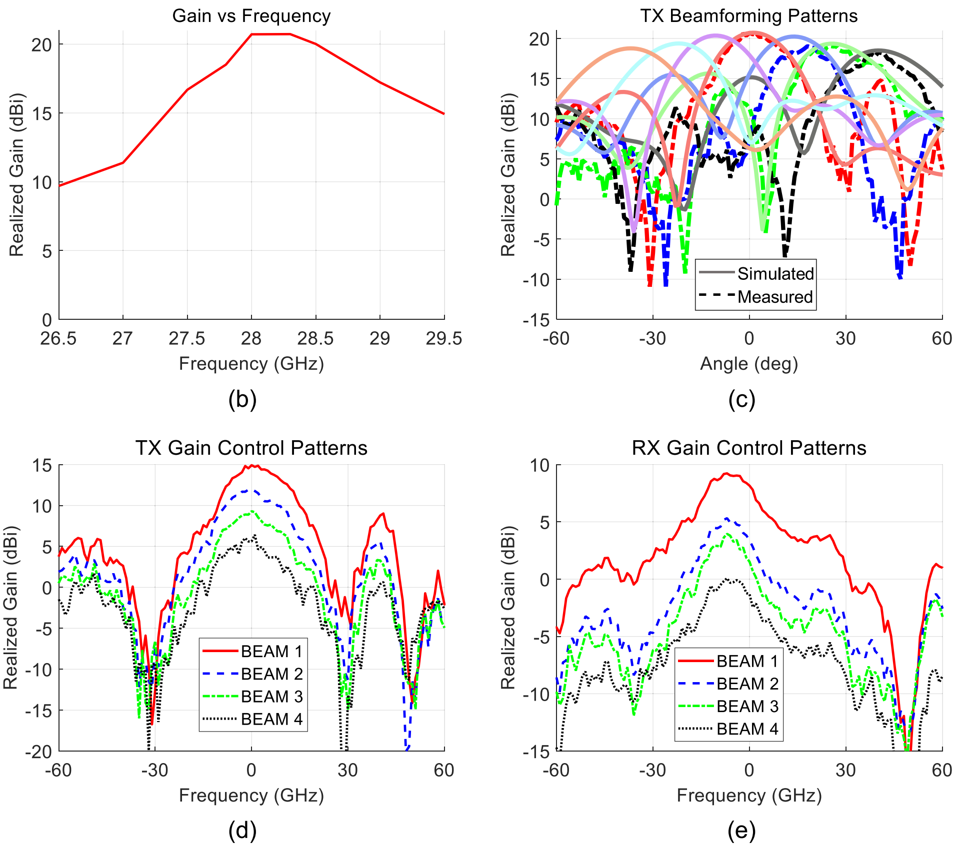

(b) (c)

(d) (e)

FIGURE 15. **(a) Distribution loss and gain at different locations in the CoD POC component at 28 GHz. (b) Measured system gain as a function of operating frequency. (c) Measured and simulated beamsteering radiation patterns in the TX mode at 28 GHz. Measured gain control radiation patterns in the TX mode (d) and RX mode (e) at 28 GHz.**

matrix is assigned to the beamformer MMIC by the serial peripheral interface for electronically-controlled beamsteering operation. All far-field radiation patterns of the CoD POC are measured with the ON state of the OLED panel. This cellular handset prototype with the CoD POC is positioned above the antenna jig of the mmWave anechoic chamber (Fig. 8(a)) for accurate measurement.

The gain and loss of the TX channel from the RF common port to the output ports of RF channels are summarized as shown in Fig. 15(a) and take into account the ohmic and power dividing loss. The well-established three-antenna method [36] is employed to perform gain calibration measurements. Therefore, the gain of the CoD POC can be measured using the known loss and gain characteristics of each component. In order to measure the CoD POC containing four RF ports, the beamformer MMIC which can accurately distribute power to each port is configured in the measurement environment. RF characteristics of the beamformer MMIC and assembly cables/connectors are carefully extracted by conduction test using the Keysight UXA N9040B signal analyzer and Keysight E8267D signal generator. The laser alignment finder is utilized to improve the positional accuracy of the antenna under test (AUT) in the far-field chamber setup. A piece of foam is used to support the CoD POC and minimize the coupling effect from the sample holder. The designed PAs of the beamformer MMIC feature an output P_{1dB} of 6 dBm and P_{SAT} of 7 dBm at 28 GHz. The measured peak PA gain of the RF package is 24.9 dB including power-combing loss in four RF channels. The total ohmic loss is 8.22 dB and composed of 6.72 dB for ohmic transmission-line loss and 1.5 dB for bond and mismatching loss between the RF package and the FPCB. The characteristics of the MMIC are summarized and compared with the latest relevant works in Table 2. The estimated RF package gain is calculated using the measured results of

TABLE 2. **Comparison With State-of-the-Art Mmwave Phased-array Transceiver ICs**

Reference	This work	UCSD '17 [37]	IBM’ 18 [38]
Process	28nm LP CMOS	0.18 μm SiGe BiCMOS	0.13 μm SiGe BiCMOS
Chip area (mm^2)	20.5	11.7	165.9
Frequency (GHz)	28	28	28
Single path RF gain TX/RX (dB)	28.5/25	20/20	34/35
VGA gain control TX/RX (dB)	22/17	14/14	8/8
Phase resolution (°)	45	5.625	5
RMS phase error (°)	3.16	3.4	0.8
TX OP_{sat} / OP_{1dB} / el. (dBm)	7/6	12.5 / 10.5	16 / 13.5
RX NF / chip (dB)	5.5	4.6	6
TX power dissipation / el. (mW)	375 @ P_{1dB}	200 @ P_{1dB}	143.8
RX power dissipation / el. (mW)	62.5	130	103.1

TABLE 3. **Comparison With State-of-the-Art Mmwave Phased-array AiPs**

Reference	This work	Samsung '17 [39]	Qualcomm' 18 [40]
Type	CoD	AiP	AiP
Antenna Placement	Inside the display panel	Top and bezel region	Backcover of cellular handsets
IC integration level	RF front-end	RF front-end + RF/IF conversion	RF front-end
Frequency (GHz)	28	60	28
Elements in Array	4	4	8
Beam scanning angles (°)	± 40	± 40	± 45
Touch operation	Yes	No	No

each component excluding the antenna array gain. Fig. 15(b) illustrates the measured system gain in the TX mode over the frequency range 26.5–29.5 GHz for the CoD POC when the four elements are fully activated. A measured peak gain of 20.72 dB and a maximum estimated EIRP of 8.82 dBm are achieved at 28 GHz.

Four antenna elements with 6.23 mm center-to-center spacing between adjacent elements are activated to verify the beamforming capability of the CoD POC. The phase distribution of the RF port excitation and corresponding scanning angles are summarized in Table 1. The measured radiation patterns (Fig. 15(c)) of the CoD POC confirm a beamsteering range of ±40° in azimuth plane without any phased array calibration. Moreover, it is meaningful that these beamsteering radiation patterns are formulated through the use of phase shifters featuring only 3-bit resolutions. It is worth noting that despite the scenario where the finger model is located upon the front glass and is centered above the first element, the antenna array of the HEMS circuit has demonstrated acceptable beam steering characteristics in different scanning angles from −30° to 48°. In addition, the MIMO array configuration can be constructed using a combination of multiple phased arrays of the HEMS circuit and phased array AiPs which are already configured in current mobile devices. This MIMO array configuration not only increases the spectral efficiency of the entire system through spatial multiplexing but also reduces the effect of human blockage through spatial diversity technology. Gain control of the CoD POC is exemplified in both TX and RX modes, as illustrated in Fig. 15(d) and (e). It should be noted that these gain control radiation patterns are achieved without any calibration technology or tapering the power supplied to each port. Therefore, sidelobe level (SLL) can be further suppressed by optimizing the weighting matrix of the input port of each RF channel.

Table 3 summarizes the performance comparison with recently reported mmWave phased-array AiPs for cellular applications. It should be noted that the proposed CoD is the first to report touch display-integrated mmWave phased-array RF front-end which can enhance the beamforming coverage in the foreside direction of cellular handsets.

VI. CONCLUSION

This article presents a flexible, invisible HEMS which can be seamlessly integrated within touch display panels such as OLED and LCD panels. Denoted as CoD, this approach is the first to combine electroquasistatic and electromagnetic sensors onto a single layer. While new display-driven designs are gaining momentum, these innovations pose unprecedented challenges to the implementation of advanced microwave circuits and systems for 5G and beyond wireless devices. The HEMS topology is exemplified to dually function as a radio-frequency transceiver and a high-resolution touch screen display with electromagnetic shielding capability, which paves the way for the development of future emerged devices. The CoD POC featuring optical transparency of more than 88% has demonstrated the beamforming capability with a system gain of 20.7 dB and a scanning angle of ±40° in azimuth plane without any phased array calibration. Concurrently, the touch sensor remains intact despite the inclusion of the CoD within the display panel. The wave-trapped circuit has been introduced for the antennas and touch sensors of the HEMS circuit to achieve high noise immunity against external EMI noises. The reported results highlight the potential of engineering new advanced technologies on display platforms and provide a starting point for seamless integration of various electromagnetic sensors within display panels for future 6G wireless, radar, and sensing scenarios.

REFERENCES

[1] K. K. Kim, I. Ha, P. Won, D.-G. Seo, K.-J. Cho, and S. H. Ko, “Transparent wearable three-dimensional touch by self-generated multiscale structure,” *Nature Commun.,* vol. 10, no. 1, pp. 1–8, 2019.

[2] P. Bhagwat, “Bluetooth: Technology for short-range wireless apps,” *IEEE Internet Comput.,* vol. 5, no. 3, pp. 96–103, May/Jun. 2001.

[3] E. Ferro and F. Potorti, “Bluetooth and wi-fi wireless protocols: A survey and a comparison,” *IEEE Wireless Commun.,* vol. 12, no. 1, pp. 12–26, Feb. 2005.

[4] S. Kasera and N. Narang, *3G Mobile Networks*. New York, NY, USA, USA: McGraw-Hill Education, 2004.

[5] E. Dahlman, S. Parkvall, and J. Skold, *4G, LTE-Adovanced Pro and the Road to 5G*, 3rd ed. Cambridge, MA, USA: Academic, 2016.

[6] A. Gupta and R. K. Jha, “A survey of 5G network: Architecture and emerging technologies,” *IEEE Access,* vol. 3, pp. 1206–1232, Jul. 2015.

[7] E. G. Larsson, O. Edfors, F. Tufvesson, and T. L. Marzetta, “Massive MIMO for next generation wireless systems,” *IEEE Commun. Mag.,* vol. 52, no. 2, pp. 186–195, Feb. 2014.

[8] X. Liu *et al.*, “Beam-oriented digital predistortion for 5G massive MIMO hybrid beamforming transmitters,” *IEEE Trans. Microw. Theory Techn.,* vol. 66, no. 7, pp. 3419–3432, Jul. 2018.

[9] B. Yang, Z. Yu, J. Lan, R. Zhang, J. Zhou, and W. Hong, “Digital beamforming-based massive MIMO transceiver for 5G millimeter-wave communications,” *IEEE Trans. Microw. Theory Techn.,* vol. 66, no. 7, pp. 3403–3418, Jul. 2018.

[10] B. M. Lee and H. Yang, “Massive MIMO with massive connectivity for industrial Internet of Things,” *IEEE Trans. Ind. Electron.,* vol. 67, no. 6, pp. 5187–5196, Jun. 2020.

[11] J. Choi, W. Hwang, C. You, B. Jung, and W. Hong, “Four-element reconfigurable coupled loop MIMO antenna featuring LTE full-band operation for metallic-rimmed smartphone,” *IEEE Trans. Antennas Propag.,* vol. 67, no. 1, pp. 99–107, Jan. 2019..

[12] A. Ren and Y. Liu, “A compact building block with two shared-aperture antennas for eight-antenna MIMO array in metal-rimmed smartphone,” *IEEE Trans. Antennas Propag.*, vol. 67, no. 10, pp. 6430–6438, Oct. 2019.

[13] P. Bahramzy *et al.*, “A tunable RF front-end with narrowband antennas for mobile devices,” *IEEE Trans. Microw. Theory Techn.*, vol. 63, no. 10, pp. 3300–3310, Oct. 2015.

[14] W. Hong, K.-H. Baek, Y. Lee, Y. Kim, and S.-T. Ko, “Study and prototyping of practically large-scale mmWave antenna systems for 5G cellular devices,” *IEEE Commun. Mag.*, vol. 52, no. 9, pp. 63–69, Sep. 2014.

[15] S. Shakib, J. Dunworth, V. Aparin, and K. Entesari, “mmWave CMOS power amplifiers for 5G cellular communication,” *IEEE Commun. Mag.*, vol. 57, no. 1, pp. 98–105, Jan. 2019.

[16] M. Stanley, Y. Huang, H. Wang, H. Zhou, A. Alieldin, and S. Joseph, “A transparent dual-polarized antenna array for 5G smartphone applications,” in *Proc. IEEE Int. Symp. Antennas Propag. USNC/URSI Nat. Radio Sci. Meet.*, Boston, MA, USA, Jul. 2018, pp. 635–636.

[17] L. Zhou, A. Wanga, S.-C. Wu, J. Sun, S. Park, and T. N. Jackson, “All-organic active matrix flexible display,” *Appl. Phys. Lett.*, vol. 88, no. 8, 2006, Art. no. 083502.

[18] T. Sekitani *et al.*, “Stretchable active-matrix organic light-emitting diode display using printable elastic conductors,” *Nature Mater.,* vol. 8, no. 6, pp. 494–499, Jun. 2009.

[19] M. Noda *et al.*, “An OTFT-driven rollable OLED display,” *J. Soc. Inf. Display,* vol. 19, no. 4, pp. 316–322, Apr. 2011.

[20] N. Savage, “Tomorrow’s industries: From OLEDs to nanomaterials,” *Nature,* vol. 576, no. 7786, pp. S20–S22, Dec. 2019.

[21] J. Park, S. Y. Lee, J. Kim, D. Park, W. Choi, and W. Hong, “An optically invisible antenna-on-display concept for millimeter-wave 5G cellular devices,” *IEEE Trans. Antennas Propag.,* vol. 67, no. 5, pp. 2942–2952, May 2019.

[22] J. Park *et al.*, “OLED display-integrated optically invisible phased arrays for millimeter-wave 5G cellular devices,” in *Proc. IEEE MTT-S Int. Microw. Symp.*, Los Angeles, CA, USA, Aug. 2020, pp. 699–702.

[23] M. El Halaoui, L. Canale, A. Asselman, and G. Zissis, “An optically transparent antenna integrated in OLED light source for 5G applications,” in *Proc. IEEE Int. Conf. Environ. Electr. Eng., IEEE Ind. Commer. Power Syst. Eur.*, Madrid, Spain, Jun. 2020, pp. 1–5.

[24] R. Rodríguez-Cano, S. Zhang, and G. F. Pedersen, “Transparent mm-Wave array on a glass substrate with surface wave reduction,” in *Proc. 14th Eur. Conf. Antennas Propag.*, Copenhagen, Denmark, Mar. 2020, pp. 1–4.

[25] S. Kim *et al.*, “A highly sensitive capacitive touch sensor integrated on a thin-film-encapsulated active-matrix OLED for ultrathin displays,” *IEEE Trans. Electron Devices,* vol. 58, no. 10, pp. 3609–3615, Oct. 2011.

[26] E. Karrer and U. Smith, “Diffusion of light from a searchlight beam,” *J. Opt. Soc. Amer.,* vol. 7, no. 12, pp. 1211–1234, 1923.

[27] S. K. Sharma, A. Lüttgen, and C. D. Sarris, “On the integration of antennas with touch sensor panels,” in *Proc. IEEE Int. Symp. Antennas Propag. USNC/URSI Nat. Radio Sci. Meet.*, Atlanta, GA, USA, Jul. 2019, pp. 707–708.

[28] S. K. Sharma, A. Lüttgen, B. R. Mehta, and C. Sarris, “Electromagnetically-aware design of capacitive touch sensor panel electrodes for antenna integration,” *IEEE Sensors J.*, vol. 20, no. 18, pp. 10633–10642, Sep. 2020.

[29] K. Lim, K.-S. Jung, C.-S. Jang, J.-S. Baek, and I.-B. Kang, “A fast and energy efficient single-chip touch controller for tablet touch applications,” *IEEE J. Display Technol.,* vol. 9, no. 7, pp. 520–526, Jul. 2013.

[30] A. Lüttgen, S. K. Sharma, D. Zhou, D. Leigh, S. Sanders, and C. D. Sarris, “A fast simulation methodology for touch sensor panels: Formulation and experimental validation,” *IEEE Sensors J.,* vol. 19, no. 3, pp. 996–1007, Feb. 2019.

[31] M. D. Tenuta and L. W. Bokma, “Touch sensor panel calibration,” U.S. Patent 8 890 854, Nov. 18, 2014.

[32] E. Song, H.-B. Park, and H. H. Park, “An evaluation method for radiated emissions of components and modules in mobile devices,” *IEEE Trans. Electromagn. Compat.,* vol. 56, no. 5, pp. 1020–1026, Oct. 2014.

[33] C. Hwang *et al.*, “LCD baseband noise modulation estimation for radio frequency interference in mobile phones,” in *Proc. IEEE Asia-Pac. Int. Symp. Electromagn. Compat.*, Seoul, South Korea, Jun. 2017, pp. 226–228.

[34] C.-L. Lin, P.-C. Lai, P.-C. Lai, T.-C. Chu, and C.-L. Lee, “Bidirectional gate driver circuit using recharging and time-division driving scheme for in-cell touch LCDs,” *IEEE Trans. Ind. Electron.,* vol. 65, no. 4, pp. 3585–3591, Apr. 2018.

[35] D. Sievenpiper, L. Zhang, R. F. J. Broas, N. G. Alexopolous, and E. Yablonovitch, “High-impedance electromagnetic surfaces with a forbidden frequency band,” *IEEE Trans. Microw. Theory Techn.*, vol. 47, no. 11, pp. 2059–2074, Nov. 1999.

[36] K. Selvan, “Preliminary examination of a modified three-antenna gain-measurement method to simplify uncertainty estimation,” *IEEE Antennas Propag. Mag.*, vol. 45, no. 2, pp. 78–81, Apr. 2003.

[37] K. Kibaroglu, M. Sayginer, and G. M. Rebeiz, “A low-cost scalable 32-Element 28-GHz phased array transceiver for 5G communication links based on a 2 × 2 beamformer flip-chip unit cell,” *IEEE J. Solid-State Circuits*, vol. 53, no. 5, pp. 1260–1274, May 2018.

[38] B. Sadhu *et al.*, “A 28-GHz 32-element TRX phased-array IC with concurrent dual-polarized operation and orthogonal phase and gain control for 5G communications,” *IEEE J. Solid-State Circuits*, vol. 52, no. 12, pp. 3373–3391, Dec. 2017.

[39] W. Hong, K.-H. Baek, and S. Ko, “Millimeter-wave 5G antennas for smartphones: Overview and experimental demonstration,” *IEEE Trans. Antennas Propag.*, vol. 65, no. 12, pp. 6250–6261, Dec. 2017.

[40] J. D. Dunworth *et al.*, “A 28 GHz bulk-CMOS dual-polarization phased-array transceiver with 24 channels for 5G user and basestation equipment,” in *Proc. IEEE Int. Solid-State Circuits Conf.*, Feb. 2018, pp. 70–71.